Molecular alloying drives valence change in a van der Waals antiferromagnet

Frédéric Aribot[1†], Laura Voigt[1†], Maja A. Dunstan[1], Wenjie Wan[2], James N. McPherson[1], Mariusz Kubus[1], Nathan J. Yutronkie[3], Charles J. McMonagle[4,9], Marco Coletta[5], Anna S. Manvell[1], Anton Viborg[1], Siena Wong[1], Kirstine A. Stampe, Volodymyr Baran[6], Anatoliy Senyshyn[6], Manh Duc Le[7], Helen C. Walker[7], Amit Chanda[8], Felix Trier[8], Nini Pryds[8], Fabrice Wilhelm[3], Michael R. Probert[4], Niels B. Christensen[2], Euan K. Brechin[5], Andrei Rogalev[3] & Kasper S. Pedersen[1]✉

Bespoke van der Waals (vdW) crystals provide control over the generation, confinement, and transport of charge, spin, light, and heat within and between atomically precise two-dimensional (2D) layers. We report a novel functionality in vdW crystals by actuating valence changes in a metal-organic antiferromagnet through molecular alloying. The quadratic net materials $Cr(pyz)_2Br_2$ and $Cr(pyz)_2I_2$ (pyz = pyrazine) are aliovalent, with different Cr(III) and Cr(II) oxidation states due to disparate crystal field potentials induced by I^- and Br^-. Applying isotropic pressure compresses the layers in $Cr(pyz)_2I_2$ significantly (16% at 1.5 GPa), but no Cr valence change is induced by mechanical strengthening of the axial crystal field. However, the alloyed, solid solutions $Cr(pyz)_2I_{2-x}Br_x$ exhibit quantitative, hysteretic, and tunable Cr(II) ⇄ Cr(III) interconversions with concomitant charge injection into the organic scaffold. This valence change, driven by the larger chemical pressure exerted by Br^- over I^-, manifests drastic changes to the magnetization and electrical conductivity, which varies by up to five orders of magnitude across the transition. The use of reticular coordination chemistry addresses a current gap in vdW and 2D materials science, where electronic structure engineering via valence change events has remained elusive. The concept of molecular alloying in vdW crystals expands the functionalities for future magnetoelectronics with drastically different electronic and magnetic states interchangeable by mild external stimuli.

Since the discovery of graphene, the science of 2D magnetic materials and their stacked analogues, van der Waals (vdW) crystals, has been rapidly evolving.[1,2,3] Breakthroughs such as 2D long-range and layer-dependent magnetic order in CrI_3 and $Cr_2Ge_2Te_6$ have made this field one of the most promising avenues of condensed matter research.[4,5,6] However, modulation of the electronic structure, the spin state, and the ensuing magnetic properties through electron transfer events via external stimuli remains elusive in vdW and related 2D materials. The possibilities for electronic structure engineering in such materials are fundamentally hindered by the simplicity of the chemical composition of all known, entirely inorganic materials candidates. The confluence of inorganic and organic materials in reticular chemistry[7] hosts the potential to unlock new vistas for property engineering at the molecular and atomic level in vdW crystals. Control of entangled geometric and electronic structure, central to coordination chemistry, presents a method to engineer reticular vdW crystals with chemically encoded valence change (*tautomeric*, VT) transitions. These transitions are well-known in inorganic materials, where a temperature or pressure trigger leads to, for example, insulator–metal transitions,[8] or the emergence of superconductivity.[9] Despite such possibilities for reshaping and tuning materials

[1]Department of Chemistry, Technical University of Denmark, Kgs. Lyngby (Denmark). [2]Department of Physics, Technical University of Denmark, Kgs. Lyngby (Denmark). [3]European Synchrotron Radiation Facility, BP 220, 38043 Grenoble Cedex 9 (France). [4]Chemistry, School of Natural and Environmental Sciences, Newcastle University, Newcastle upon Tyne (United Kingdom). [5]School of Chemistry, The University of Edinburgh, Edinburgh (United Kingdom). [6]FRM-II, Technical University of Munich, Garching (Germany). [7]ISIS Neutron and Muon Source, Rutherford Appleton Lab. Laboratory, Chilton (United Kingdom). [8]Department of Energy Conversion and Storage, Technical University of Denmark, Kgs. Lyngby (Denmark). [9]Present address: Swiss-Norwegian Beamlines, European Synchrotron Radiation Facility, 71 Avenue des Martyrs, 38000 Grenoble, France.

†These authors contributed equally to this work. ✉e-mail: kastp@kemi.dtu.dk

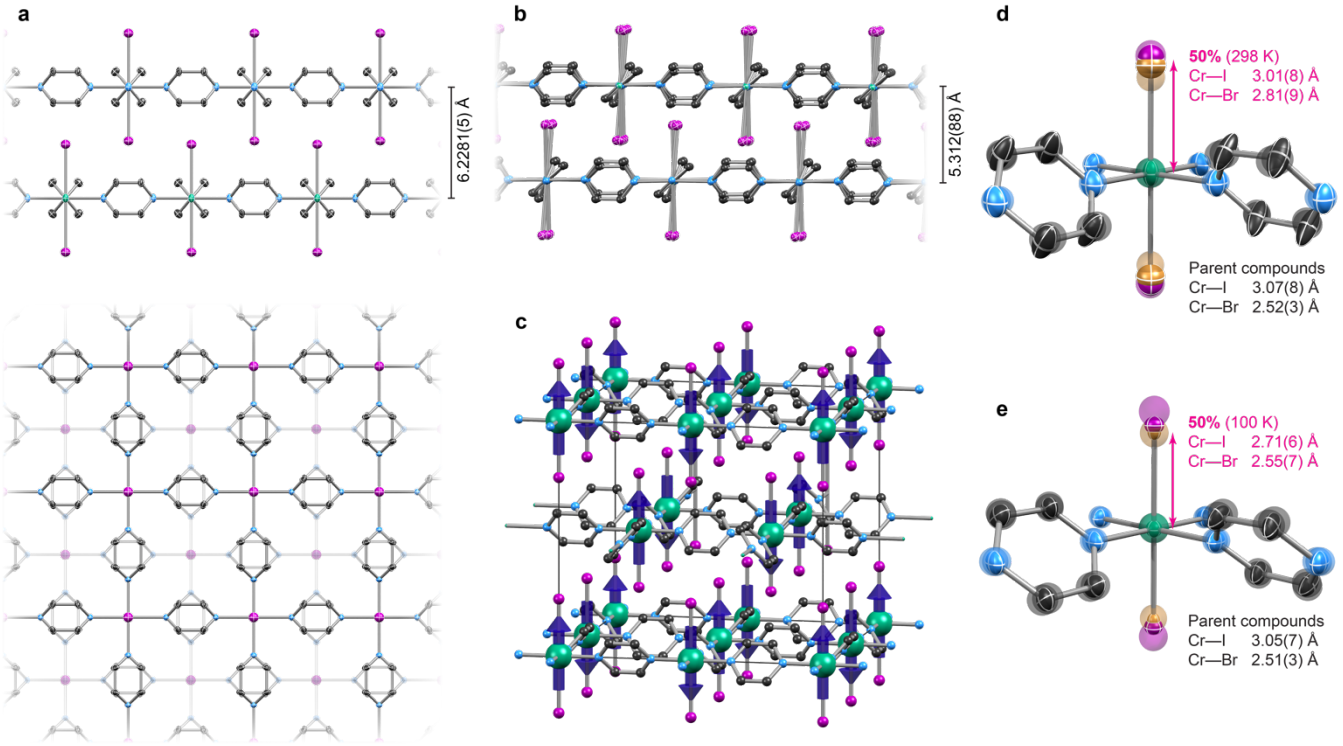

Fig. 1 | Two perpendicular views of two 3 × 3 layer fragments of $Cr(pyz)_2I_2$ (**0%**) from its single-crystal X-ray diffraction structure (298 K) and at ambient pressure (**a**, top: view down $\vec{a}$, bottom: view down $\vec{c}$) and at 1.54 GPa (**b**, view down $\vec{b} + \vec{c}$). **c**, Unit cell of the magnetic structure of $Cr(pyz)_2I_2$ (**0%**). **d** and **e**, Solid ellipsoids: 3D-ED structure of $Cr(pyz)_2IBr$ (**50%** at 298 K (**d**) and at 100 K (**e**)), overlaid onto the atomic positions from 3D-ED structures of $Cr(pyz)_2I_2$ (**0%**) and $Cr(pyz)_2Br_2$ (**100%**) obtained under identical conditions. Color codes: green, Cr; orange, Br; purple, I; blue, N; black, C. Hydrogen atoms are omitted for clarity.

properties, VT phenomena have not yet been observed in vdW crystals. In the vdW antiferromagnet $FePSe_3$, the application of pressure leads to emergent superconductivity,[10,11] tied to a localized spin-crossover transition at the Fe(II) ion. Subsequent theoretical studies suggest that the isostructural, but hitherto unobtainable, $CrPS_3$ may be subject to a pressure-induced VT transition rather than spin crossover, with a concomitant switch from an antiferro- to a ferromagnetic phase.[12] Fundamental to the observation of the VT phenomenon stands the energy alignment of the electron donor and acceptor units. Whilst difficult to control in inorganic materials, where the VT transition involves the promotion of a localized electron to the conduction band or vice versa, coordination chemistry uniquely allows tailoring of electron transfer between metal ions and organic ligands.[13,14] The spontaneous electron transfer between Cr(II) and pyrazine (pyz) has been known for decades,[15] but has recently been a key factor in the development of layered conductive magnets,[16] and magnets with exceptional magnetic hardness and critical temperatures.[17,18,19] Chemically related systems, with no apparent electron transfer events, are instead electrically insulating antiferromagnets.[20,21] The dichotomy in properties stems fundamentally from the redox-activity in the organic scaffold being actuated or not, and developing a handle on this mechanism provides a novel route to establish stimuli-dependent switching of metal-organic vdW crystals. Here, we tailor switchable magnetic and electrical properties of a square-lattice vdW antiferromagnet using the concept of molecular alloying.

The self-assembly reaction of $Cr(thf)_3I_2$ (thf = tetrahydrofuran) with pyrazine led to the immediate formation of microcrystalline $Cr(pyz)_2I_2$. Single-crystal X-ray diffraction revealed $Cr(pyz)_2I_2$ to be an ideal tetragonal net of pyz-bridged {*trans*-CrI_2} units (Fig. 1a, Supplementary Table 1,2). Although the structure is similar to the previously reported, orthorhombic net $Cr(pyz)_2Cl_2$,[16] no indications of a crystallographic symmetry lower than tetragonal could be identified for $Cr(pyz)_2I_2$. The long, Jahn-Teller-distorted Cr—I bond of 3.0534(9) Å (298 K; *cf.* Cr—I of 3.0816(4) Å in $Cr^{II}I_2(CH_3CN)_4$ and 2.655(2)–2.692(2) in $Cr^{III}I_3(CH_3CN)_3$, ref. 22) suggests the presence of Cr(II) in $Cr(pyz)_2I_2$, as opposed to Cr(III) in the $Cr(pyz)_2Cl_2$ prototype.[16] The magnetic susceptibility–temperature (χT) product of $Cr(pyz)_2I_2$ amounts to 2.4 cm^3 K mol^{-1} at 300 K and decreases steadily upon cooling, indicative of dominant antiferromagnetic superexchange interactions between the high-spin Cr(II) centers (Fig. 2a). The $\chi(T)$ displays a maximum at 20 K and below $T_{Néel} \approx 25$ K, $\chi(T)$ becomes magnetic field-dependent (Supplementary Fig. 13). The 4 K powder neutron diffraction pattern shows weak, additional reflections compared to the diffractogram at 60 K (Supplementary Fig. 17) unveiling an antiferromagnetically ordered ground state structure with a propagation vector (1/2, 1/2, 0) and an ordered Cr moment of 1.8(3) μ_B, oriented along the crystallographic *c* axis (Fig. 1c).

The magnetic excitation spectrum, determined using powder time-of-flight inelastic neutron scattering (INS), displays dispersive spin-wave excitations in the energy range of 1–4.5 meV (Fig. 3a). The dispersion minima occur at momenta, Q, that are consistent with the propagation vector determined from neutron powder diffraction, most prominently at $Q \approx 0.62$ Å^{-1}, corresponding to $\mathbf{Q} = (1/2, 1/2, 0)$. The magnetic nature of the excitations is corroborated by their decrease in intensity with increasing Q, and by their temperature dependence, which shows the closure of an anisotropy gap and gradual loss of definition of the dispersive features when the temperature exceeds $T_{\text{Néel}}$ (Supplementary Fig. 18). The salient features of the low-temperature spin wave spectrum can be modelled using a 2D square-lattice Heisenberg model given by the Hamiltonian

$$H = J\sum_{\langle i,j\rangle}\vec{S}_i\cdot\vec{S}_j \;+ D\sum_i (S_i^z)^2$$

with a nearest neighbor exchange interaction of $J = 0.51(1)$ meV and Cr(II) single-ion magnetic anisotropy reflected by $D = -0.06(2)$ meV (Fig. 3b). A fit of $\chi^{-1}(T)$ to the Curie-Weiss law ($\chi^{-1} = (T - \theta)/C$) affords a Curie constant of $C = 2.7$ cm^3 K mol^{-1}, close to that of an uncorrelated high-spin Cr(II) ion with $g = 2.0$ (3.0 cm^3 K mol^{-1}), and a Weiss temperature of $\theta = -37$ K (Fig. 2a, inset). Calculating θ using the J extracted from INS affords $\theta \approx -4JS(S+1)/3k_B = -46$ K, in good agreement with the magnetization data.[23] Encouraged by the apparent disparity of the electronic and magnetic properties of $Cr(pyz)_2I_2$ and the previously reported $Cr(pyz)_2Cl_2$,[16] the analogous $Cr(pyz)_2Br_2$ was pursued. Attempts to grow single crystals systematically led to the isolation of orthorhombic $Cr(pyz)_2Br_2$ isomorphous to, and with similar physical properties as $Cr(pyz)_2Cl_2$.[24] However, the rapid reaction of an acetonitrile–dimethylformamide solution of $Cr(thf)_2Br_2$ with molten pyrazine resulted in the formation of a tetragonal phase of $Cr(pyz)_2Br_2$, isomorphous to $Cr(pyz)_2I_2$ (Supplementary Fig. 11). Given the submicron crystal sizes, the structure was determined by 3D electron diffraction (3D-ED, Supplementary Fig. 5, 6, Supplementary Tables 1, 3). The Cr—Br bond length (298 K) of 2.52(3) Å is synonymous with a Cr(III) oxidation state assignment. In stark contrast to the behavior of $Cr(pyz)_2I_2$, the χT product increases upon cooling from room temperature (RT, Fig. 2a), but no remanent magnetization is observed down to 2 K (Supplementary Fig. 15).

The X-ray absorption spectra (XAS) acquired around the Cr K-edge energy of $Cr(pyz)_2I_2$ and $Cr(pyz)_2Br_2$ demonstrate a ~1 eV and ~2.5 eV shift of the pre-edge and rising edge, respectively, confirming the higher oxidation state of Cr in $Cr(pyz)_2Br_2$ (Fig. 4, Supplementary Fig. 19). Single-crystal X-ray diffraction analysis of $Cr(pyz)_2I_2$ (120 K) and 3D-ED analysis of $Cr(pyz)_2Br_2$ (100 K) reveal only minor thermal contractions (Supplementary Fig. 3 and 5, Supplementary

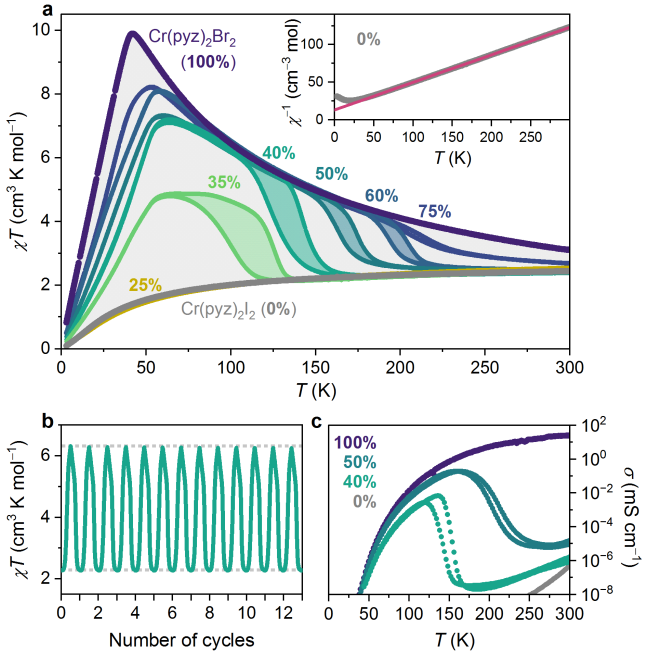

Fig. 2 | a, Temperature dependence of the susceptibility–temperature product, χT, ($\mu_0 H$ = 0.1 T, sweeping rate = 1 K min^{-1}) for the pristine $Cr(pyz)_2I_2$ (**0%**) and $Cr(pyz)_2Br_2$ (**100%**), and the alloys, $Cr(pyz)_2I_{2-x}Br_x$, labeled according to their percental Br content (**0%–100%**). The data for **25%** coincides with those of $Cr(pyz)_2I_2$. The inset shows the $\chi^{-1}(T)$ and the corresponding fit to the Curie-Weiss law (red line) for $Cr(pyz)_2I_2$ (**0%**). **b**, Temperature cycling between 180 K and 90 K for **40%** (1.5 K min^{-1}). **c**, Temperature dependence scans of the electrical conductivity for **0%**, **40%**, **50%**, and **100%**. Supplementary Figs 14–16 contain additional magnetization data for the series.

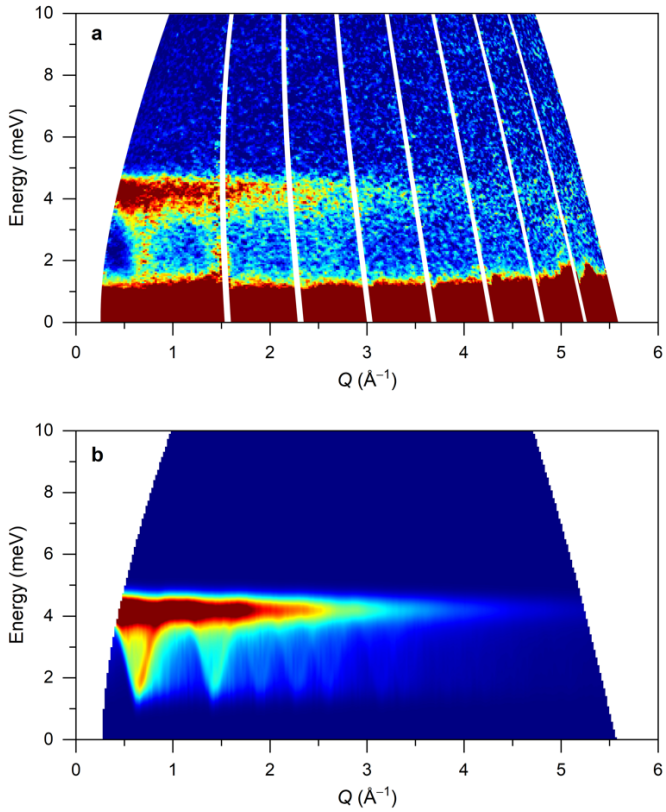

Fig. 3 | a, Time-of-flight INS spectrum of polycrystalline, fully deuterated $Cr(pyz\text{-}d_4)_2I_2$ (6 K, incident neutron energy of 19 meV). **b**, Simulated powder INS cross section using the 2D Heisenberg model discussed in the main text.

Table 1–3), and the absence of any changes in Cr oxidation state upon cooling is confirmed by XAS at 50 K (Supplementary Fig. 20). This analysis suggests that the critical ligand field strength to actuate valence change resides between the Br^- and I^- in the spectrochemical series. Given the layered nature of the crystals (Fig. 1a), application of an isotropic pressure would be expected to compress the crystals predominantly along the stacking *c* direction, thereby leading to an increase in the axial component of the crystal field. A high-pressure single-crystal X-ray structure of $Cr(pyz)_2I_2$ was determined at 1.54 GPa (Fig. 1b). The pressure induces a contraction of the interlayer distance of 16% from 6.297(2) Å at ambient pressure to 5.31(9) Å at 1.54 GPa, and a phase transition from tetragonal $I4/mmm$ to monoclinic $C2/c$. The compression leads to a distortion of the coordination sphere with now nonlinear I—Cr—I (172.25(8)°) and slight deviations of the N—Cr—N angles from the 90° found at ambient pressure. In contrast, the bond lengths are virtually unaltered compared to the ambient pressure structure (Cr—I 3.092(2) Å, Cr···Cr 7.0073(3) Å, and Cr—N 2.15(1) Å, 2.16(1) Å), suggesting the conservation of the Jahn-Teller distorted coordination environment and a Cr(II) oxidation state.

To induce a facile VT transition, we increased the *chemical* pressure by doping $Cr(pyz)_2I_2$ with Br^- to yield mixed-halide $Cr(pyz)_2I_{2-x}Br_x$ materials, as a strategy to obtain phases verging on even thermal valence instabilities. A similar "molecular alloying" approach was introduced by Kahn to tune the transition temperature in 1D spin-crossover materials over a wide temperature range.[25] The coordination self-assembly reaction using a one-to-one ratio of $Cr(thf)_2Br_2$ and $Cr(thf)_3I_2$ afforded a microcrystalline powder. Elemental analysis confirms the formulation $Cr(pyz)_2IBr$ (**50%**) and powder X-ray diffraction suggests a phase isomorphous to that of the pristine phases (Supplementary Fig. 8–10). The 3D-ED structure at 298 K could be solved as a $Cr(pyz)_2X_2$ phase with 50% Br and 50% I at the *X* position of the asymmetric unit (Fig. 1d). No indications of a larger supercell could be found, suggesting either a random distribution of the X^- ions or homo-halide $\{CrX_2\}$ units in **50%**. The Cr—*X* bond lengths in **50%** at 298 K (Cr—I: 3.01(8) Å, Cr—Br: 2.81(9) Å), are consistent with the Cr—I bond (3.07(8) Å) found in the 3D-ED structure of pristine $Cr(pyz)_2I_2$ (hereafter referred to as **0%**) at 298 K. At 100 K, however, the Cr—*X* bonds in **50%** are considerably shorter (Fig. 1e, Cr—I: 2.71(6) Å, Cr—Br: 2.55(7) Å), and much closer to the Cr—Br bonds (2.51(3) Å) found in $Cr(pyz)_2Br_2$ (hereafter **100%**) at 100 K. This structural analysis indicates the occurrence of a temperature-driven VT transition in a single nanocrystal grain. Additional $Cr(pyz)_2I_{2-x}Br_x$ alloys were synthesized with Br concentrations between 25% and 75%, all of which were found to consist of a single phase by RT powder X-ray diffraction analysis (Supplementary Fig. 11). The evolution of the unit cell parameters, as determined from Rietveld refinements, deviates significantly from linearity in doping concentration (Supplementary Fig. 12). The low Br content alloys exhibit unit cell parameters similar to **0%** with growing differences approaching the parameters of **100%** as the Br content increases (Supplementary Table S4).

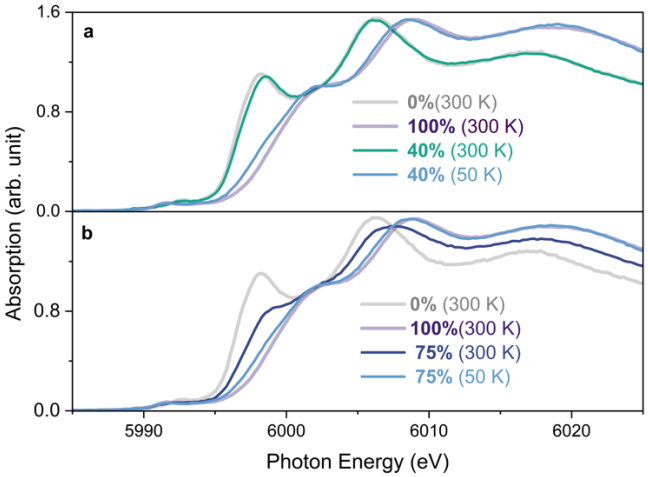

Fig. 4 | Cr K-edge X-ray absorption spectra of **0%**, **100%**, and **40%** (panel **a**) and **75%** (panel **b**).

The χT product of **50%** at 300 K is close to that of **0%**, indicative of a formal Cr(II) oxidation state (Fig. 2a). However, upon cooling the χT product exhibits an abrupt increase at the critical temperature $T_c\downarrow$ = 162 K (Fig. 2a, as defined by the inflection point of $\chi T(T)$) and upon further cooling, the χT product closely follows that of **100%**. Upon reheating, the χT product decreases precipitously at $T_c\uparrow$ = 175 K. This hysteretic thermal response of the χT product is attributed to a Cr(II) ⇄ Cr(III) transition, with a concomitant redox event in the pyrazine scaffold. The phase transition is resistant to fatigue, with repeated cycling experiments across the phase transition demonstrating only a ~1% of change in the χT values after thirteen cycles (Fig. 2b). Across the family of alloys, the values of $T_c\uparrow$ and $T_c\downarrow$ are strongly sensitive to the Br doping percentage and changes by *ca.* 100 K (Fig. 2a).

To further support the existence of VT transitions, XAS were complementarily recorded at 300 K and 50 K for the **75%** and **40%** alloys (Fig. 4a). For **40%**, the 300 K spectrum superposes perfectly to that of **0%**, while the 50 K spectrum closely resembles that of **100%**. Warming back to 300 K leads to a full recovery of the initially recorded 300 K spectrum (Supplementary Fig. 20). These observations confirm the conclusions drawn from magnetometry and demonstrate a complete VT transition in **40%**. On the contrary, in **75%**, the 300 K spectrum appears as a linear combination of the spectra of **0%** and **100%**, suggesting the coexistence of Cr(II) and Cr(III) in **75%** at room temperature (Fig. 4b). Upon cooling to 50 K, the spectrum of **75%** overlaps perfectly with the spectrum of **100%**, reflecting the full conversion to the Cr(III) state. Br K-edge XAS studies corroborate this conclusion. **100%** exhibits a clear pre-edge shoulder (13488 eV; Supplementary Figs 23–26) which, at RT, decreases and eventually vanishes with decreasing Br doping concentration. This spectral feature is assigned to transitions from core 1*s* states into vacancies in the Br 4*p* levels, originating from the increased Cr–Br covalency in Cr(III) over Cr(II). Upon cooling to 50 K, the pre-edge feature increases in intensity, as expected for a Cr(II) → Cr(III) VT transition.

The Cr(III) oxidation state in **100%** is synonymous with a mixed valency in the organic scaffold, formally constituting equal proportions of neutral pyz and $pyz^{\bullet-}$. This situation has been at the origin of high electrical conductivity in the related $M(pyz)_2Cl_2$ (M = Cr, Ti) phases.[16,26] Electrical resistivity measurements reveal **100%** to be a semiconductor with σ_{RT} = 25 mS cm^{-1} (Fig. 2c). In contrast, **0%** displays at least eight orders of magnitude lower conductivity ($\sigma_{RT} = 5 \times 10^{-7}$ mS cm^{-1}), consistent with the inactivation of pyrazine-scaffold mixed valency. The **40%** and **50%** alloys are also largely insulating at RT (~1×10^{-6} and ~1×10^{-5} mS cm^{-1}, respectively), however, upon cooling their conductivities increase drastically around the VT transition, which for **40%** results in an increase in σ of five orders of magnitude. At lower temperatures, $\sigma(T)$ for **40%** and **50%** reaches and follows that of **100%**, reflecting the similar electronic structures.

Thermally driven switchability in magnetic vdW crystals and 2D materials has previously only been observed in molecule-based nets showing spin crossover.[27] In molecule-based materials, such metal ion-centered interconversions of spin states do not lead to any significant modulation of the extended 2D layers' electronic structure. Thus, the primary interest has focused on utilizing the volumetric change associated with the transition to induce strain in vdW heterostructures.[28] Akin to the spin-crossover mechanism, the electron transfer from Cr(II) to organic ligands with empty π^* orbitals was recently found to be controllable by the axial component of the crystal field, that raises the energy of the singly occupied $3d_{z^2}$ orbital located along the Jahn-Teller axis.[29] The $Cr(pyz)_2X_2$ alloys constitute unique vdW crystal analogues in which molecular switching can be exploited. The crystallographic, spectroscopic, magnetization, and resistivity data univocally support the existence of a complete VT transition in the $Cr(pyz)_2X_2$ alloys, but the complete absence of any VT in the pristine $Cr(pyz)_2I_2$ and $Cr(pyz)_2Br_2$. Despite the presence of $\{Cr(pyz)_4I_2\}$, $\{Cr(pyz)_4Br_2\}$, and the potential presence of $\{Cr(pyz)_4IBr\}$ coordination environments in the alloys, of which the first two would be expected to host Cr(II) and Cr(III), respectively, the VT transition happens cooperatively and involves all Cr centers. Whilst $Cr(pyz)_2X_2$ are still in their bulk crystalline form, the calculated exfoliation energy of related metal–pyrazine nets (0.1 J m^{-2}) is smaller than those of archetypal vdW crystals such as graphite, MoS_2, and CrI_3 (0.3–0.4 J m^{-2}), suggesting that dimensionality reduction in these materials may be feasible.[30] This is further supported by recent, initial results on the exfoliation of related Fe(II)–pyrazine nets.[31]

In conclusion, this work establishes a new paradigm in the manipulation of metal-organic vdW crystals, where molecular alloying can drive complete VT transitions from parent materials that do not display any VT transition themselves. Indeed, the very concepts of molecular alloying may be transferable also to the entirely inorganic vdW crystals, heralding a new era of responsive 2D materials. Molecule-based frameworks, however, exhibit significantly greater flexibility compared to inorganic materials and, consequently, are anticipated to produce substantial responses to mechanical stress. The close energetic proximity of the distinct valence states suggests that the molecular alloys may be switchable by gating or strain, implying the potential for next-generation electronic and spintronic applications, where precise control over charge and spin is paramount.

Methods

Synthesis. All manipulations and sample preparations took place inside an InertLab glovebox (H_2O, O_2 < 0.5 ppm) under inert Ar atmosphere or with Schlenk line techniques. A Puresolv MD 7 solvent purification system was used for provision of dry and air-free solvents. Elemental analyses were obtained at the Mikroanalytisches Laboratorium Kolbe (Oberhausen, Germany).

Synthesis of $Cr(thf)_3I_2$: Cr powder (8.10 g, 156 mmol) was added to degassed, aqueous HI (57%, 70 mL), which was subsequently heated to 100 °C for 2 h. Afterwards, the water was evaporated, and the solid product was dried at 160 °C under vacuum overnight before placing the dark brown solid (46.2 g) in the glove box. About a quarter of the crude CrI_2 (12 g) was dissolved in thf (*ca.* 400 mL) and the solution was filtered to remove insoluble impurities. The filtrate was concentrated to 100 mL and placed in the freezer (–30 °C) overnight for $Cr(thf)_3I_2$ to crystallize. The dark supernatant was pipetted off and replaced by about 40 mL fresh, cold (–30 °C) thf three times. The supernatant was collected for a second crystallization. Pale-green crystals of $Cr(thf)_3I_2$ were filtered and washed with a small amount of cold (–30 °C) thf and dried under vacuum. Yield 11.2 g (53%). Anal. calcd. (found) for $C_{12}H_{24}CrI_2O_3$: C, 27.60% (27.97%); H, 4.63% (4.73%); Cr, 9.96% (9.81%); I, 48.61% (47.89%). The $Cr(thf)_3I_2$ could also be synthesized in an alternative way: Cr powder (0.41 g, 7.8 mmol) and I_2 (2.0 g, 7.8 mmol) were ground together, placed in an ampoule (V = 21 mL), sealed under vacuum and heated to 550 °C for 50 hours. After cooling to room temperature, the ampoule was opened in the glovebox and the dark red-brown, crude CrI_2 was stirred in thf (15 mL) for 5 min before being filtered. This process was repeated twice, and the combined filtrates were cooled to –30 °C. After one night, a first crop of pale-green crystals of $Cr(thf)_3I_2$ were isolated by filtration (1.1 g, 2.1 mmol). The filtrate was concentrated *in vacuo* to 15 mL and cooled to –30 °C, resulting in a second batch of $Cr(thf)_3I_2$ crystals (420 mg, 0.8 mmol). Yield 1.5 g (38 %).

Synthesis of $Cr(thf)_2Br_2$: $CrBr_3$ (2.5 g, synthesized as described in ref. [32]) was loaded on a quartz boat and placed in a horizontal tube furnace. The furnace was heated to 200 °C for 30 min under a dry Ar stream. Afterwards a constant stream of H_2 in He (10%) was introduced, and the furnace was heated to 600 °C for 6 h. The reaction was then cooled to room temperature and quickly transferred to a dried Schlenk flask, evacuated and back filled with Ar. The light green crude product was transferred to a glove box, where it was dissolved in thf (*ca.* 400 mL) under slight heating and the solution was filtered to remove insoluble impurities. The filtrate was concentrated to *ca.* 100 mL and left in the freezer (–30 °C) overnight for $Cr(thf)_2Br_2$ to crystallize. Pale crystals of $Cr(thf)_2Br_2$ were collected by filtration and washed with a small amount of cold thf (–30 °C). The filtrate was used for a second crystallization. Yield: 2.2 g (72%). The crystal structure

was identified as the same as previously reported, where the compound was obtained as a side-product.[33] Anal. calcd. (found) for $C_8H_{16}CrBr_2O_2$: C, 26.99% (27.41%); H, 4.53% (4.61%); Cr, 14.61% (14.39%); Br, 44.89% (44.19%).

Synthesis of $Cr(pyz)_2I_2$ (0%): A boiling solution of $Cr(thf)_3I_2$ (52.2 mg, 100 μmol) in acetonitrile (2.5 mL) was added dropwise to a melt (85 °C) of pyrazine (300 mg, 3.7 mmol), yielding a dark grey precipitate almost immediately. The resulting mixture was cooled to room temperature (5 min), concentrated under vacuum, filtered by suction, and washed with acetonitrile (2 × 2 mL). After drying under vacuum, a dark grey solid could be isolated. Yield: 44 mg (95%). Anal. calcd. (found) for $C_8H_8CrI_2N_4$: C, 20.62% (20.53%); H: 1.73% (1.85%); I, 54.47% (54.04%); N: 12.02% (11.87%). Single-crystals (up to 0.2 mm) suitable for single-crystal X-ray diffraction analysis were obtained in an ampoule (V = 21 mL), which was filled with $Cr(thf)_3I_2$ (0.10 g, 0.19 mmol) and pyrazine (1.0 g, 12.5 mmol). After sealing under vacuum, the ampoule was, over the course of 5 h, heated to 200 °C, kept at this temperature for 80 h, and subsequently cooled to room temperature over 20 h. The sample contained a mixture of dark grey crystals and microcrystalline powder, which were washed with acetonitrile (20 mL) and isolated by vacuum filtration. Yield: 67 mg (75% based on Cr). The same method was utilized to synthesize the fully deuterated analogue $Cr(pyz\text{-}d_4)_2I_2$.

Synthesis of $Cr(pyz)_2Br_2$ (100%): A warm solution of $Cr(thf)_2Br_2$ (35.6 mg, 100 μmol) in acetonitrile (2.5 mL) and dmf (two drops) was added dropwise to a melt (65 °C) of pyrazine (300 mg, 3.7 mmol), yielding a dark precipitate almost immediately. The resulting mixture was cooled to room temperature over 5 min, filtered under vacuum and washed with acetonitrile (2 × 2 mL). After drying a microcrystalline, dark purple solid could be isolated. Yield: 34 mg (92%). Anal. calcd. (found) for $C_8H_8N_4CrBr_2$: C, 25.83% (26.78%); H, 2.17% (2.25%); Br, 42.96% (41.69%); N, 15.06% (15.62%).

Synthesis of $Cr(pyz)_2IBr$ (50%): A warm solution of $Cr(thf)_2Br_2$ (17.8 mg, 50 μmol) and $Cr(thf)_3I_2$ (26.1 mg, 50 μmol mmol) in acetonitrile (2.5 mL) was added dropwise to a melt (65 °C) of pyrazine (300 mg, 3.7 mmol), yielding a dark precipitate almost immediately. The resulting mixture was cooled to room temperature, filtered under vacuum and washed with acetonitrile (2 × 2 mL). After drying, a dark purple microcrystalline solid could be isolated in essentially quantitative yield. Anal. calcd. (found) for $C_8H_8N_4CrIBr$: C, 22.93% (22.84%); H, 1.92% (1.97%); Br, 19.07% (19.02%); Cr, 12.41% (12.34%); I, 30.29% (30.11%); N, 13.37% (13.31%). The $Cr(pyz)_2I_{2-x}Br_x$ alloys were synthesized following an analogous procedure (for **75%**, two drops of dimethylformamide aided the dissolution and the precursors and a reaction temperature of 55 °C was used) and obtained with similar yields in the following ratios: **75%**: $Cr(thf)_2Br_2$ (26.7 mg, 75 μmol) $Cr(thf)_3I_2$ (13.0 mg, 25 μmol). Anal. calcd. (found) for $C_8H_8N_4CrI_{0.5}Br_{1.5}$: Br, 30.31% (29.89%); I, 16.04% (15.81%); C, 24.30% (24.72%); N, 14.17% (14.41%); H, 2.04% (2.07%). **60%**: $Cr(thf)_2Br_2$ (21.3 mg, 60 μmol), $Cr(thf)_3I_2$ (21 mg, 40 μmol). Anal. calcd. (found) for $C_8H_8N_4CrI_{0.8}Br_{1.2}$: Br, 23.41% (23.28%); I, 24.79% (24.53%). **40%**: $Cr(thf)_2Br_2$ (14.2 mg, 40 μmol), $Cr(thf)_3I_2$ (31.3 mg, 60 μmol). Anal. calcd. (found) for $C_8H_8N_4CrI_{1.2}Br_{0.8}$: Br, 14.92% (14.72%); I, 35.55% (35.07%); C, 22.43% (22.94%); N, 13.08% (13.38%); H, 1.88% (1.93%). **35%**: $Cr(thf)_2Br_2$ (12.4 mg, 35 μmol), $Cr(thf)_3I_2$ (33.9 mg, 65 μmol). Anal. calcd. (found) for $C_8H_8N_4CrI_{1.3}Br_{0.7}$: Br, 12.91% (12.48%); I, 38.09% (36.91%); C, 22.19% (23.30%); N, 12.94% (13.59%); H, 1.86% (1.96%). **25%**: $Cr(thf)_2Br_2$ (8.9 mg, 25 μmol), $Cr(thf)_3I_2$ (39.1 mg, 75 μmol). Anal. calcd. (found) for $C_8H_8N_4CrI_{1.5}Br_{0.5}$: Br, 9.03% (8.92); I, 43.02% (42.79)

X-ray crystallography. Single crystals of $Cr(thf)_3I_2$ (120 K) and $Cr(pyz)_2I_2$ (120 K and 298 K) were immersed in polybutene oil (Sigma-Aldrich, >90%), mounted onto a nylon loop, and then measured under an N_2 stream with a SuperNova Dual Source CCD-diffractometer using Mo Kα radiation. Olex2[34] was used for structure solution with direct methods using the ShelXS structure solution program and the structure was refined by Least Squares in the version 2018/3 of ShelXL.[35] Non-hydrogen atoms were refined anisotropically. Single-crystal X-ray diffraction of $Cr(pyz)_2I_2$ under high pressure was conducted at the School of Chemistry, University of Newcastle (Newcastle, United Kingdom). A single crystal of $Cr(pyz)_2I_2$ was selected and loaded into a diamond anvil cell (DAC) with a hydrostatic medium of Daphne oil and pressurized to 1.54 GPa using ruby as a pressure calibrant.[36] The data were then collected on a Bruker D8 Venture laboratory diffractometer using Ag Kα radiation. The phase transition from the ambient to the high-pressure structure was partially destructive, leading to a splitting of the single crystal into multiple domains under pressure. The shading from the DAC and the low symmetry, monoclinic unit cell, led to lower than ideal completeness. Every attempt was made to maximize the quality of data obtained. Four major domains were identified, and the data was integrated as a twin using SAINT and TWINABS for the absorption correction. Olex2[34] was used to solve and refine the structure. The solution was made using ShelXT[40] with the merged HKLF4 and the refinement was carried out using ShelXL and the unmerged HKLF5.[35] It was not possible to refine a fully anisotropic non-hydrogen model for these data. The low completeness in a specific direction is due to the systematic shading from the DAC. This gives little information on the lighter elements of the pyrazine ring in one direction leading to unreasonable ADPs in a fully anisotropic refinement. Therefore, it was deemed more appropriate to isotropically refine this whole group leaving only the heavier elements, Cr and I, as anisotropic.

Powder X-ray diffraction. Powder X-ray diffraction patterns were obtained at ambient temperature using Cu Kα radiation (λ = 1.5406 Å) in transmission geometry on a Malvern Panalytical Empyrean powder X-ray diffractometer equipped with a 1Der detector. The powders were packed into borosilicate capillaries (∅ 0.7 mm) within an Ar-filled glovebox, sealed with grease, and flame-sealed outside the glovebox. All Rietveld refinements were performed in the HighScore Plus 5.1.0 program suite.[37] All structures were refined against the room-temperature $Cr(pyz)_2I_2$ single-crystal X-ray structure and the peak profiles were fitted using a pseudo-Voigt peak shape function. All atomic positions were

kept fixed, except for the halide positions, which were refined along the *c* axis (along the Cr—*X* bond), and the occupancy was changed so the I/Br ratio matched the synthetic ratios. For all refinements, a background function was determined and used. Temperature dependent powder X-ray diffraction data of **50%** were acquired on a Supernova (Oxford Diffraction) single-crystal diffractometer equipped with an Atlas CCD detector.

Electron crystallography. Continuous rotation 3D electron diffraction (3D-ED) data were acquired using a Rigaku XtaLAB Synergy-ED dedicated electron diffractometer, equipped with a Rigaku Oxford Diffraction HyPix detector.[38,39] Inside an Ar-filled glove box, microcrystalline powders of $Cr(pyz)_2I_2$ (**0%**), $Cr(pyz)_2IBr$ (**50%**), and $Cr(pyz)_2Br_2$ (**100%**) were gently ground then loaded onto continuous carbon film TEM grids. The grids were transferred into an airtight sample transfer puck which was then removed from the glovebox and into a Gatan Cold Transfer Station where it was submerged directly into liq. N_2 and opened. The grids were then mounted on a Gatan ELSA cold sample holder at ~120 K, which was then inserted into the airlock chamber of the electron diffractometer. The sample stage was then warmed gently and held at 175 K for 15 minutes to ensure any adventitious ice was sublimed off the grid before the sample was fully inserted into the column and cooled to 100 K. Data acquisition was performed using an electron wavelength of 0.0251 Å (200 keV), with continuous rotation of the crystals around a single axis (α) inside an effective 1.9 μm selected area aperture. The sample stage was then warmed to 298 K, and a second set of data was acquired at this temperature for each crystal. At the conclusion of all diffraction experiments, postmortem high-resolution images (at ×15,000 magnification) were acquired. The raw diffraction data were processed using CrysAlisPro, and the structures were solved using ShelXT.[40] The structures were refined by ShelXL[35] using a kinematical approximation in the Olex2[34] and ShelXLe[41] graphical user interfaces. Rigid body restraints were applied to the anisotropic displacement parameters and, where necessary, additional SIMU commands were applied to stabilize overlapping halide atoms. Bonds between the disordered positions of the pyrazine rings were suppressed using FREE commands, and then H atoms were placed by the appropriate AFIX instruction, using the default settings for neutron structures (which are generally more appropriate for ED). Bonds between disordered halides and symmetry generated (disordered) H atoms were also removed from the connectivity tables using appropriate FREE commands.

Magnetic measurements. Direct-current (dc) magnetization measurements were performed on polycrystalline samples sealed in QuantumDesign powder capsules with a QuantumDesign Dynacool Physical Property Measurement System (PPMS). Using the VSM option, the susceptibility was measured from 3 K to 300 K at 1 T and the magnetization versus field was measured up to 9 T. The sample masses were measured with a Mettler-Toledo WXTSDU microbalance and the experimental data were corrected for diamagnetism.

Neutron scattering. Powder diffraction patterns were measured on the high-resolution powder diffractometer SPODI of Heinz Maier-Leibnitz Zentrum (Germany), neutron wavelength λ = 2.5370 Å. A powder sample of non-deuterated $Cr(pyz)_2I_2$ was sealed in a V sample holder cans. The sample was cooled in a closed cycle cryostat with a base temperature of 4.5 K. Powder diffraction data were analyzed with MAG2POL.[42] The inelastic neutron scattering experiment was performed at the MARI spectrometer at the ISIS Neutron and Muon Source (United Kingdom). A powder sample (3.0 g) of fully deuterated $Cr(pyz\text{-}d_4)_2I_2$ was mounted in an annular geometry inside an aluminum can, which in turn was connected to the cold finger of a closed-cycle refrigerator. The data were obtained in repetition rate multiplication mode with incident neutron energies E_i = 8.7, 19, and 68.7 meV and a chopper frequency of 200 Hz, yielding calculated elastic energy resolutions 0.28, 0.78, and 3.1 meV, respectively. Data were recorded for sample temperatures 6, 15, 30, 60 and 100 K. The highest temperature data were employed for subtracting phonon contribution to the total spectrum. The raw data were processed using the Mantid software package[43] and the resulting data analyzed in MATLAB using SpinW.[44]

Electrical conductivity. Temperature-dependent electrical resistivities of $Cr(pyz)_2I_2$ (**0%**) $Cr(pyz)_2Br_2$ (**100%**), **50%**, and **40%** were measured with a Keithley 6487 picoammeter, with samples mounted in a QuantumDesign Dynacool Physical Properties Measurement System (PPMS). The samples were placed in a home-made PTFE cell and pressed between two stainless steel screws, giving sample thicknesses in the range of 0.3–0.6 mm. The cell was attached to a QuantumDesign dc resistance puck, with each terminal connected to the corresponding screw via Cu wire, and the cell fastened to the puck with thermal varnish, mounted in the PPMS for temperature control. The PPMS was connected to the picoammeter via a custom Aivon BoBoX breakout box, and controlled using a homebuilt code in the LabView software. Measurements were obtained with a current limit of 25 mA, excitation voltage of 10 V, and averaged over 10–30 measurements per data point. Temperature sweeps were performed at 1–2 K min^{-1} to allow for thermalization of the sample.

X-ray spectroscopy. X-ray absorption spectra (XAS) at the K-edges of Cr and Br were recorded on powder samples in flame-sealed quartz capillaries (∅ 0.9 mm) using total fluorescence yield detection mode at the ID12 beamline at the European Synchrotron (ESRF, Grenoble, France). Spectra were normalized using standard procedures and were corrected for reabsorption effects.

Data availability

Crystallographic data for the structures reported in this article have been deposited at the Cambridge Crystallographic Data Centre, under deposition numbers CCDC 2367722–2367739. Copies of the data can be obtained free of charge via https://www.ccdc.cam.ac.uk/structures/. Raw inelastic neutron scattering data are available at https//doi.org/10.5286/ISIS.E.RB1920693.

Acknowledgements

K.S.P. thanks the Villum Foundation for a VILLUM Young Investigator grant, a VILLUM Young Investigator+ (42094) grant, and the Independent Research Fund Denmark for a DFF-Sapere Aude Starting Grant (no. 0165-00073B), and the Carlsberg Foundation for a research infrastructure grant (no. CF17-0637). A.C. and F.T. acknowledge support by research grant 37338 (SANSIT) from Villum Foundation. This work was supported by the Danish National Committee for Research Infrastructure (NUFI) through the ESS-Lighthouse Q-MAT. N.P. acknowledge the support of Novo Nordisk Foundation Challenge Pro-gramme 2021: Smart nanomaterials for applications in life-science, BIOMAG Grant NNF21OC0066526 and the support from the ERC Advanced "NEXUS" Grant 101054572. E.K.B. thanks the EPSRC (EP/V010573/1, EP/P025986/1, EP/N01331X/1) and Leverhulme Trust (RPG-2021-176) for funding. M.R.P. thanks the EPSRC (grant EP/W021129/1) for continued support of the diffraction facilities. The X-ray spectroscopy experiments were performed at the ID12 beamline at the European Synchrotron Radiation Facility (Grenoble, France). Experiments at the ISIS Neutron and Muon Source were supported by beamtime allocation RB1920693 from the Science and Technology Facilities Council. The authors thank the Technical University of Denmark for funding the DTU Electron Crystallography Facility, and the Danish Agency for Science, Technology, and Innovation for funding the instrument centre "Danscatt".

Author contributions

K.S.P. conceived and supervised the project. F.A., L.V., M.A.D., A.V., and S.W. synthesized and chemically characterized the materials. L.V., J.N.M., M.K., F.A., A.M., and K.S.P. performed the ambient pressure powder- and single-crystal X-ray and electron crystallographic analysis. C.J.M., M.C., M.R.P., and E.K.B. performed the high-pressure crystallographic experiments and analysis. K.S.P., L.V., F.A., M.A.D., and W.W. obtained and analyzed the magnetization data. M.A.D., A.C., F.T., K.S.P., and N.P. obtained and analyzed the resistivity data. L.V., W.W., M.K., K.A.S., V.B., A.S., M.D.L., H.C.W., and N.B.C. acquired and analyzed the neutron diffraction and time-of-flight neutron scattering data. N.J.Y., F.W., and A.R. recorded and interpreted the X-ray absorption data. The manuscript was written by K.S.P., F.A., M.A.D., and J.N.M. through contributions from all authors. All authors have consented to the publication of the manuscript.

Competing interests

The authors declare no competing interests.

[1] Burch, K. S., Mandrus, D. & Park. J.-G. Magnetism in two-dimensional van der Waals materials. *Nature* **47**, 47–52 (2018).
[2] Wang, Q. H. et al. The Magnetic Genome of Two-Dimensional van der Waals Materials. *ACS Nano* **16**, 6960–7079.
[3] Jiang, X., Liu, Q., Xing, J., Liu, N., Guo, Y., Liu. Z. & Zhao, J. Recent progress on 2D magnets: Fundamental mechanism, structural design and modification. *Appl. Phys. Rev.* **8**, 031305 (2021).
[4] Gong, C. et al. Discovery of intrinsic ferromagnetism in two-dimensional van der Waals crystals. *Nature* **546**, 265–269 (2017).
[5] Huang, B. et al. Layer-dependent ferromagnetism in a van der Waals crystal down to the monolayer limit. *Nature* **546**, 270–273 (2017).
[6] Wang, Q. H. et al. The Magnetic Genome of Two-Dimensional van der Waals Materials. *ACS Nano* **16**, 6960–7079 (2022).
[7] Jiang, H., Alezi, D. & Eddaoudi, M. A reticular chemistry guide for the design of periodic solids. *Nat. Rev. Mater.* **6**, 466–487 (2021).
[8] Yamaoka, H. et al. Unified understanding of the valence transition in the rare-earth monochalcogenides under pressure. *Phys. Rev. B* **87**, 115107 (2013).
[9] Song, J., Fabbris, G., Bi, W., Haskel, D. & Schilling, J. S. Pressure-Induced Superconductivity in Elemental Ytterbium Metal. *Phys. Rev. Lett.* **121**, 037004 (2018).
[10] Haines, C. R. S., Coak, M. J., Wildes, A. R., Lampronti, G. I., Liu, C., Nahai-Williamson, P., Hamidov, H., Daisenberger, D. & Saxena, S. S. Pressure-Induced Electronic and Structural Phase Evolution in the van der Waals Compound $FePS_3$. *Phys. Rev. Lett.* **121**, 266801 (2018).
[11] Wang, Y. et al. Emergent superconductivity in an iron-based honeycomb lattice initiated by pressure-driven spin-crossover. *Nat. Commun.* **9**, 1914 (2018).
[12] Sen, D. & Saha-Dasgupta, T. Pressure-tuned valence transition, insulator-metal transition in van der Waals antiferromagnet $CrPS_3$. *Phys. Rev. Mater.* **7**, 064008 (2023).
[13] Sato, O. Dynamic molecular crystals with switchable physical properties. *Nat. Chem.* 8, 644–656 (2016).
[14] Gransbury, G. K. & Boskovic, C. "Valence Tautomerism in d-block complexes" in *Encyclopedia of Inorganic and Bioinorganic Chemistry*, John Wiley & Sons, Ltd., pp. 1–24, Wiley (2021).
[15] Dunne, T. G. & Hurst, J. K. Kinetic and thermodynamic properties of chromium(III) complexes containing pyrazine radical ligands. *Inorg. Chem.* **19**, 1152–1157 (1980).
[16] Pedersen, K. S. et al. Formation of the layered conductive magnet $CrCl_2(pyrazine)_2$ through redox-active coordination chemistry. *Nat. Chem.* **10**, 1056–1061 (2018).
[17] Perlepe, P. et al. Molecule-based metal-organic magnets with large room-temperature coercivity and critical temperature up to 242°C. *Science* **370**, 587–592 (2020).
[18] Huang, Y., Pathak, A. K., Tsai, J.-Y., Rumsey, C., Ivill, M., Kramer, N., Hu, Y., Trebbin, M., Yan, Q. & Ren, S. Pressure-controlled magnetism in 2D molecular layers. *Nat. Commun.* **14**, 3186 (2023).
[19] Huang, Y., Zhang, Q., Li, Y. C., Yao, Y., Hu, Y. & Ren. S. Chemical Tuning Meets 2D Molecular Magnets. *Adv. Mater.* **35**, 2208919 (2022).
[20] Perlepe, P. et al. $Cr(pyrazine)_2(OSO_2CH_3)_2$: A two-dimensional coordination polymer with an antiferromagnetic ground state. *Polyhedron* **153**, 248–253 (2018).
[21] Pitcairn, J., Iliceto, A., Canadillas-Delgado, L., Fabelo, O., Liu, C., Balz, C., Weilhard, A., Argent, S. P., Morris, A. J. & Cliffe, M. J. Low-Dimensional Metal-Organic Magnets as a

Route toward the $S = 2$ Haldane Phase. *J. Am. Chem. Soc.* **145**, 1783–1792 (2023).
[22] Leigh, G. J., Sanders, J. R., Hitchcock, P. B., Fernandes, J. S. & Togrou, M. The use of trimethylsilyl iodide as a synthon in coordination chemistry. *Inorg. Chim. Acta* **330**, 197–212 (2002).
[23] Johnston, D. C. Influence of uniaxial single-ion anisotropy on the magnetic and thermal properties of Heisenberg antiferromagnets within unified molecular field theory. *Phys. Rev. B* **95**, 094421 (2017).
[24] The synthesis and properties of this phase will be reported elsewhere.
[25] Kahn, O., Sommier, L. & Codjovi, E. Spin Transition Molecular Alloys: An Attempt of Fine Tuning of the Transition Temperatures. *Chem. Mater.* **9**, 3199–3205 (1997).
[26] Perlepe, P. et el. From an antiferromagnetic insulator to a strongling correlated metal in square-lattice MCl_2(pyrazine)2 coordination solids. *Nat. Commun.* **13**, 5766 (2022).
[27] Suárez-García, S. et al. Spin-Crossover in an Exfoliated 2D Coordination Polymer and Its Implementation in Thermochromic Films. *ACS. Appl. Nano Mater.* **1**, 2662–2668 (2018).
[28] Boix-Constant, C. et al. Strain Switching in van der Waals Heterostructures Triggered by a Spin-Crossover Metal-Organic Framework. *Adv. Mater.* **34**, 2110027 (2022).
[29] Vinum, M. G., Voigt, L., Hansen, S. H., Bell, C., Clark, K. M., Larsen, R. W. & Pedersen, K. S. Ligand field-actuated redox-activity of acetylacetonate. *Chem. Sci.* **11**, 8267–8272 (2020).
[30] López-Alcalá, D., Ruiz, A. M. & Baldoví, J. J. Exploring Spin-Phonon Coupling in Magnetic 2D Metal-Organic Frameworks. *Nanomaterials* **13**, 1172 (2023).
[31] McKenzie, J., Penningtin, D. L., Kadota, K., Ericson, T., Cope, E., Cozzolini, A. F., Hendon, C. H. & Brozek, C. K. Tunable Interlayer Interactions in 2D van der Waals Frameworks. *ChemRxiv*, DOI: 10.26434/chemrxiv-2024-n5dl2 (2024).
[32] Brauer, G. Handbuch der Präparativen Anorganischen Chemie. Ferdinand Enke Verlag, Stuttgart. pp. 1174 (1962).
[33] Twamley, B., Zehnder, R. & Shapiro, P. J. Solvated $CrBr_2(Thf)_2$, a Linear Chain in the Solid State. *Acta Crystallogr. Sect. E* **57** , m80–m81 (2001).
[34] Dolomanov, O. V., Bourhis, L. J., Gildea, R. J., Howard, J. A. K. & Puschmann, H. OLEX2: A Complete Structure Solution, Refinement and Analysis Program. *J. Appl. Crystallogr.* **42**, 339–341 (2009).
[35] Sheldrick, G. M. A short history of SHELX. *Acta Crystallogr. A.* **64**, 112–122 (2007).
[36] Moggach, S. A., Allan, D. R., Parsons, S. & Warren, J. E. Incorporation of a new design of backing seat and anvil in a Merrill-Bassett diamond anvil cell. *J. Appl. Crystallogr.* **41**, 249–251 (2008).
[37] Degen, T., Sadki, M., Bron, E., König, U. & Nénert, G. The HighScore suite. *Powder Diffr.* **29**, S13–S18 (2014).
[38] Truong, K.-N. et al. Making the most of 3D Electron Diffraction: Best practices to handle a new tool. *Symmetry* **15**, 1555 (2023).
[39] Ito, S., White, F. J., Okunishi, E., Aoyama, Y., Yamano, A., Sato, H., Ferrara, J. D., Jasnowski, M. & Meyer, M. Structure Determination of Small Molecule Compounds by an Electron Diffractometer for 3D ED/MicroED. *CrystEngComm* **23**, 8622–8630 (2021).
[40] Sheldrick, G. M. SHELXT – Integrated space-group and crystal-structure determination. *Acta Crystallogr. A* **71**, 3–8 (2015).
[41] Hübschle, C. B., Sheldrick, G. M., & Dittrich, B. ShelXle: A Qt graphical user interface for SHELXL. *J. Appl. Crystallogr.* **44**, 1281–1284 (2011).
[42] Qureshi, N., *J. Appl. Crystallogr.* **52**, 175 (2019).
[43] Arnold, O. et al. Mantid – Data analysis and visualization package for neutron scattering and μSR experiments. *Nucl. Instrum. Methods Phys. Res. A* **764** 156–166 (2014).
[44] Toth, S. & Lake, B. Linear Spin-wave theory for single-Q incommensurate magnetic structures. *J. Phys.: Condens. Matter* **27**, 166002 (2015).